A. P. Alexandrov
RESEARCH INSTITUTE
OF TECHNOLOGY
N I T I

Investigation of Corium Melt Interaction With NPP Reactor Vessel Steel (METCOR) Phase 2

PROGRESS REPORT
01/01/03 – 31/03/03

STUDY OF C-30 MOLTEN CORIUM OXIDATION BY ATMOSPHERIC OXYGEN

Test Pr1-MC5/03

Project title	Investigation of Corium Melt Interaction with NPP Reactor Vessel Steel (METCOR, Phase 2), No. 833.2
Ordered by	ISTC
File specification	METCOR2/PRMB-01
Project premises	The A.P. Alexandrov Research Institute of Technology (NITI) of the Russian Atomic Energy Ministry 188540, NITI, Sosnovy Bor, Leningrad Region, Russia
Project manager	Name V.B. Khabensky Signed
	Date April, 2003

Authors

Prof.	V.B. Khabensky
Dr.	S.V. Bechta
Ph.D.	V.S. Granovsky
	S.A. Vitol
	E.V. Krushinov
Ph.D.	S.Yu. Kotova
Assoc. Acad. of RAS, Prof.	V. V. Gusarov
Prof..	Yu. B. Petrov
Ph.D.	I.V. Kulagin
Ph.D.	D.B. Lopukh
Ph.D.	A.Yu. Pechenkov
Ph.D.	I.V. Poznyak
Researcher	V.G. Bliznyuk
Engineer	V.R. Bulygin
Researcher	E.K. Kalyago
Engineer	N.E. Kamensky
Engineer	I.A. Loginov
Engineer	A.V. Lysenko
Researcher	V.I. Almyashev
Engineer	A.P. Martynov
Researcher	V.V. Martynov
	E.V. Shevchenko
Engineer	A.A. Chertkov

Contents

Introduction

The Report offers a description and main findings from the Pr1-MC5 test in the framework of the ISTC METCOR, Phase 2 Project. The research focused on the corium oxidation at replacing the inert atmosphere of melting with air. The test was performed at NITI, Sosnovy Bor, on the Rasplav-3 test facility.

The experimental objective were as follows:

- To study the possibility of molten corium superheating relative to $T_{liq.}$ at its oxidation from C-32 to C-100.
- To provide the maintenance of molten corium in superheated condition in a broad range of corium oxidation degrees.
- To study the process of suboxidized molten corium oxidation by atmospheric oxygen at replacing the inert atmosphere of melting with air.

1. Test specification

The test employed a facility featuring a high-frequency generator with 60 kW oscillating capacity and 0.13 MHz current frequency. The melt was prepared using the technique of induction melting in the cold crucible [1]. The furnace schematic diagram and appearance are shown in Fig.1.

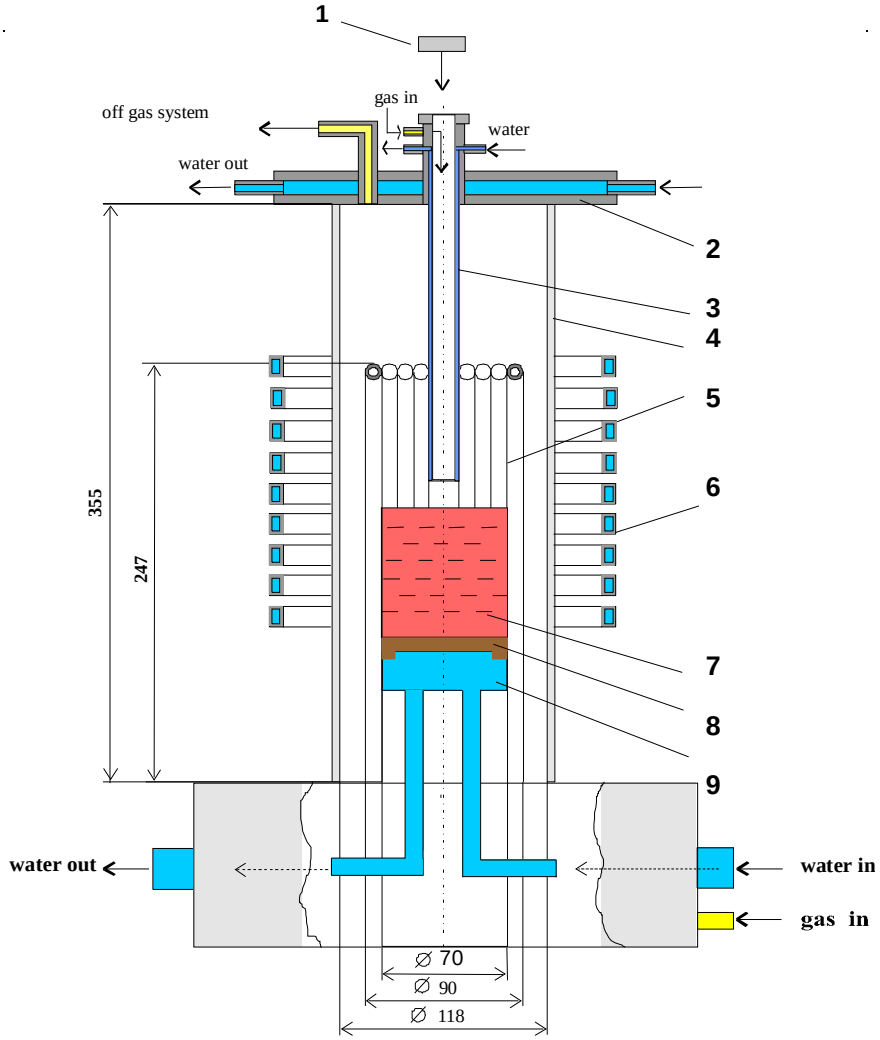

Fig.1. Furnace diagram

1 – spectral ratio pyrometer; 2 – furnace water-cooled cover;
3 – water-cooled pyrometer shaft blown through with argon; 4 – quartz tube; 5 – pipes of crucible sections; 6 -inductor; 7 – molten corium;
8 – crust; 9 – bottom calorimeter

In order to increase the power in the melt, some changes were introduced into the valve generator circuit and furnace design. The furnace was equipped with a new 10-coil generator with 70 mm internal diameter.

For determining the oxygen partial pressure in the removed gases, a system of gas supply and removal to/from the furnace was assembled (Fig. 2).

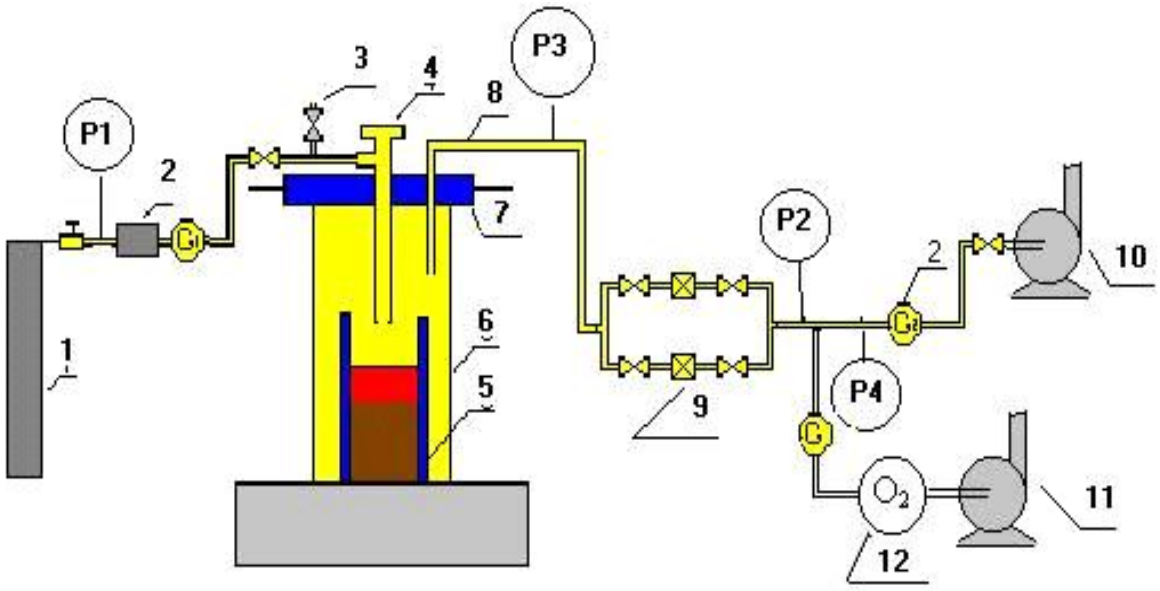

1 – argon cylinder; 2 – silica gel drier; 3 – air supply valve;
4 - pyrometer shaft blown through with argon; 5 - crucible; 6 – quartz tube,
7 – water-cooled cover; 8 – aerosol main; 9 – medium-area filters;
10-11 – vacuum pump; 12 – oxygen sensor;
P1-P4 –pressure gauges; G1-G2 – flowmeters

Fig. 2. System of gas supply and removal to/from the furnace

Medium-area filters (9), switched in turn, were used for purifying the gas from aerosols. To control such gas flow parameters as consumption and pressure, electromechanical flowmeters G1 and G2 of OR-40/S type and P1-P4 pressure gauges of 'Corund-DIV' type were placed at the locations marked by dots in the diagram. Silica gel column (2) was installed at the gas inlet to the furnace for removing traces of moisture from the gas. The gas was supplied into the furnace via shaft (4) in order to achieve a higher quality of both pyrometric measurements and video recording by blowing aerosols away.

The charge represented a mixture of powdered oxides and metallic zirconium, mass. %: 76 UO_2 + 9 ZrO_2 + 15 Zr.

To evaluate electromagnetic losses in the induction furnace components and load circuit, these elements were subjected to calorimetry during the no-load operation.

To measure heat fluxes from the molten pool to the crucible bottom, water-cooling of the latter was provided for calorimetric purposes. The test was performed in both argon and air.

2. Test description

2.1 Experimental procedure

To remove the air fixed in powders and create inert atmosphere, the furnace was blown through with argon for approximately 1,200 sec at 10 l/min. Heating was switched on and a molten pool was produced. Electrical characteristics of the HF generator and inductor, as well as pyrometer readings during the test are given in Fig. 3. The history of heat fluxes into the furnace components is shown in Fig. 4**.**

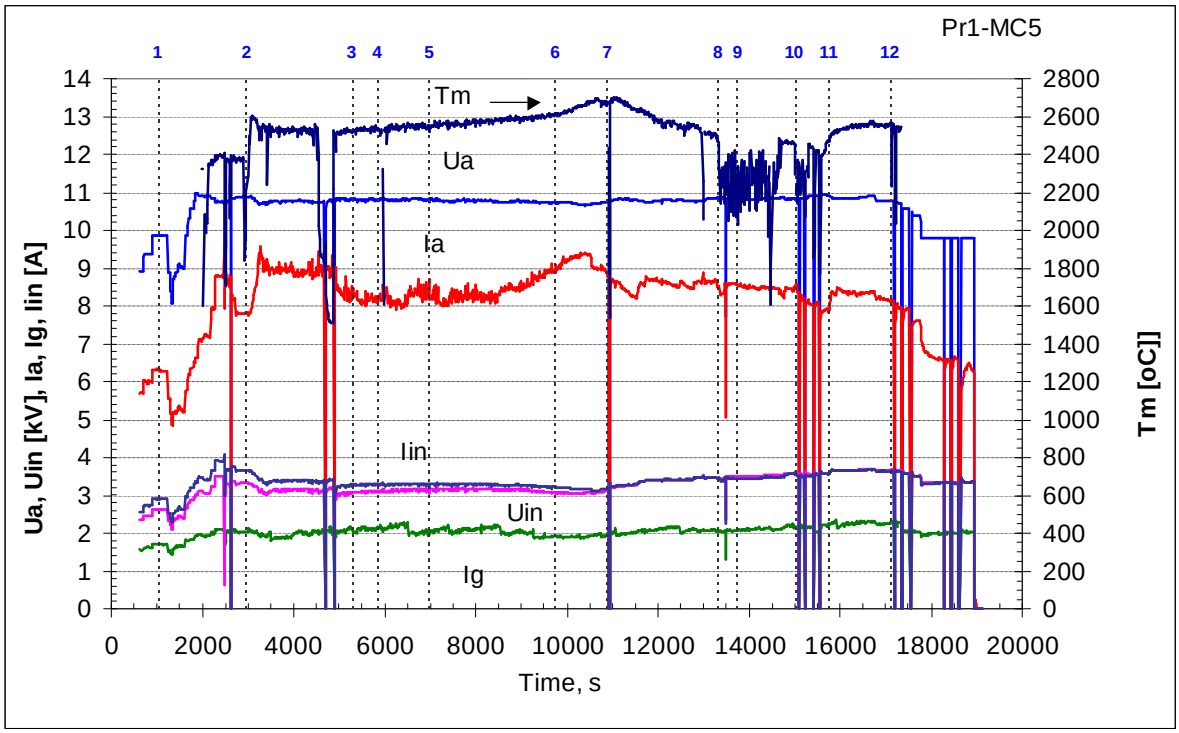

1, 4, 7 – Molten pool depth measurement; 2 – Replacement of inert atmosphere with air; Gair =2.5 l/min. 3 – Air flow rate increased, Gair=4 l/min; 5 - Gair=10 l/min; 6 - Gair=15 l/min; 8, 10, 12 – Melt sampling; 9 - Gair=24 l/min; 11 - Replacement of air with inert atmosphere.

Fig. 3. History of anode current and voltage (I_a, U_a), grid current (I_g), and inductor current and voltage (I_{in}, U_{in}), of generator frequency (f), and of pyrometer readings (T_m)

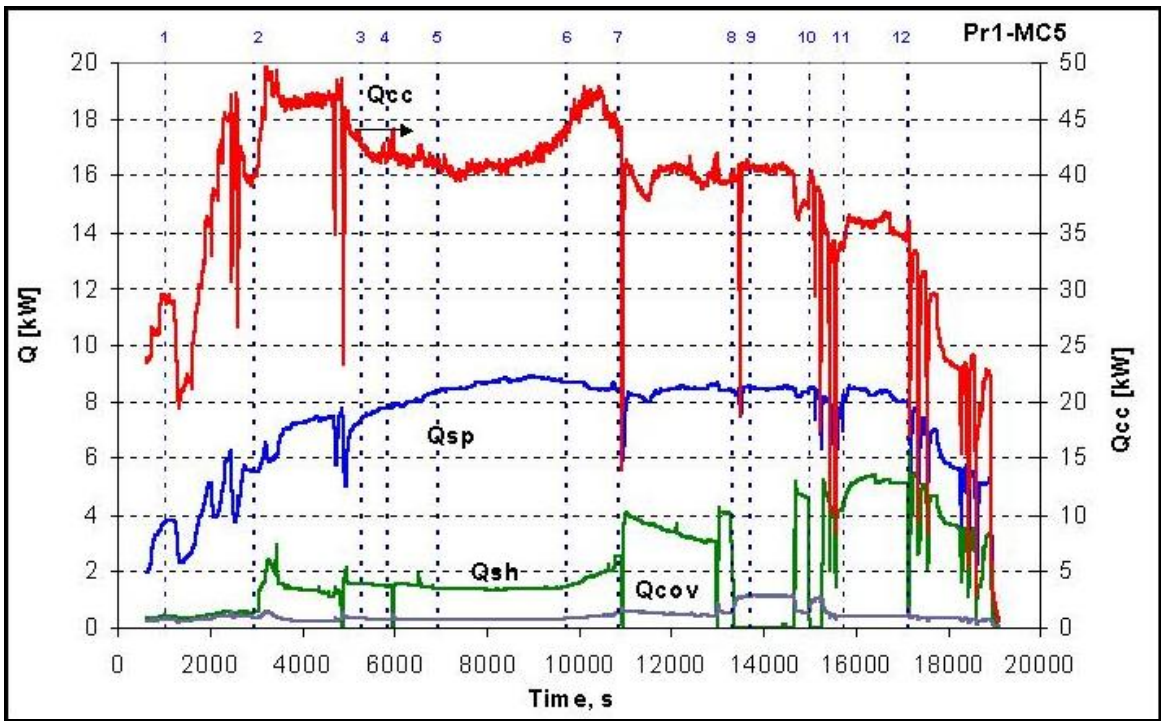

1, 4, 7 - Molten pool depth measurement; 2 - Replacement of inert atmosphere with air; Gair=2.5 l/min. 3 - Air flow rate increased, Gair=4 l/min; 5 - Gair=10 l/min; 6 - Gair=15 l/min; 8, 10, 12 - Melt sampling; 9 - Gair=24 l/min; 11 - Replacement of air with inert atmosphere.

Fig. 4. History of electromagnetic and heat losses in the crucible (Q_{cc}), inductor (Q_{in}), calorimeter (Q_{sp}), shaft (Q_{sh}), cover (Q_{cov})

Thermal equilibrium was achieved at 1,011 sec and the molten pool depth was measured with a tungsten probe. The pool depth was 54 mm and bottom crust thickness was ~ 1 mm. At 1,260 sec power in the melt was stepped down and $T_{liq.}$ was evaluated by the VPA [1]. $T_{liq.}$ of the melt was 2350±25°C.

Between 1,640-2,550 sec the power in the melt was stepped up in order determine the furnace capacity of melt superheating above $T_{liq.}$ The superheating amounted to approximately 100 °C. At 2,560 sec the coil position was adjusted in order to reduce the anode and grid currents, and after the regime of melting had stabilized, the inert atmosphere was replaced with air at 2,960 sec. The air was supplied in a stepwise manner via the pyrometer shaft placed on the furnace water-cooled cover (see Fig. 2). At the first stage, a flow rate of 2.5 l/min was maintained. Anode current growth, increase of power induced in the crucible, increase of temperature on the molten pool surface up to 2600 C, swirling and ejection of melt droplets were observed. To prevent the actuation of electronic protection, the anode current was stepped down. Later on, repeated melt ejections were observed which resulted in clogging of the pyrometer shaft from within and in accretions on the crucible sections. At 4,550 sec, when another melt ejection occurred, the breaking off of the accretions onto the melt surface caused crust formation there. At 4,800 sec the pyrometer shaft was removed from the furnace cover, the crust broken through the opening and the shaft put back in its place again.

At 5,280 sec the rate of air flow into the furnace was increased up to 4 l/min. Melt ejections leading to the formation of accretions on the crucible walls above the melt were observed again. At 5,850 sec the molten pool depth was measured with a tungsten probe. It amounted to 58 mm, while the bottom crust thickness was 3 mm. In order to remove the accretions, the shaft was removed from the furnace cover at 6,000 sec and the surfaces above the melt cleaned through the opening. At 6,940 sec the rate of air flow into the furnace was increased up to 10 l/min, and further increased up to 15 l/min at 9,720 sec. From this point up to approximately 10,550 sec, an increase of anode current at the constant anode voltage and an increase of the melt surface temperature up to 2700 °C were observed. Presumably, these phenomena were due to a reduced electrical conductivity of the melt resulting from changes in its stoichiometry. In the course of the melting, the generator valve operating regime was adjusted with the aim of maintaining its high efficiency. Starting from 10,820 sec, a decrease in anode current at the constant anode voltage was observed. Apparently, with oxidation of the melt its electrical conductivity reduces and the peak of the anode current curve corresponds to the optimal induction heating. At 10,865 sec the molten pool depth was measured and found to be 60 mm, while the bottom crust thickness was 5 mm. Later on, the melt temperature was reducing due to the changes in the generator operating regime related to the limitation of the grid and anode currents in the generator valve. A reduction of the anode current was leading to a reduction of the melt surface temperature and redistribution of power in the furnace components (see Fig. 5.

At 13,320 sec, the gas-melt equilibrium was supposed on the basis of the readings of oxygen content in the removed gas (see Fig. 5). To prove this hypothesis and determine the oxygen-total metals ratio, the melt was sampled, and at 13,720 sec the rate of air flow through the furnace was increased to 24.4 l/min. At 15,000 sec the melt was sampled again. After 15,100 sec, thermal stability of the melting was checked by de-energizing the generator several times for 5, 10, 15 and 20 sec.

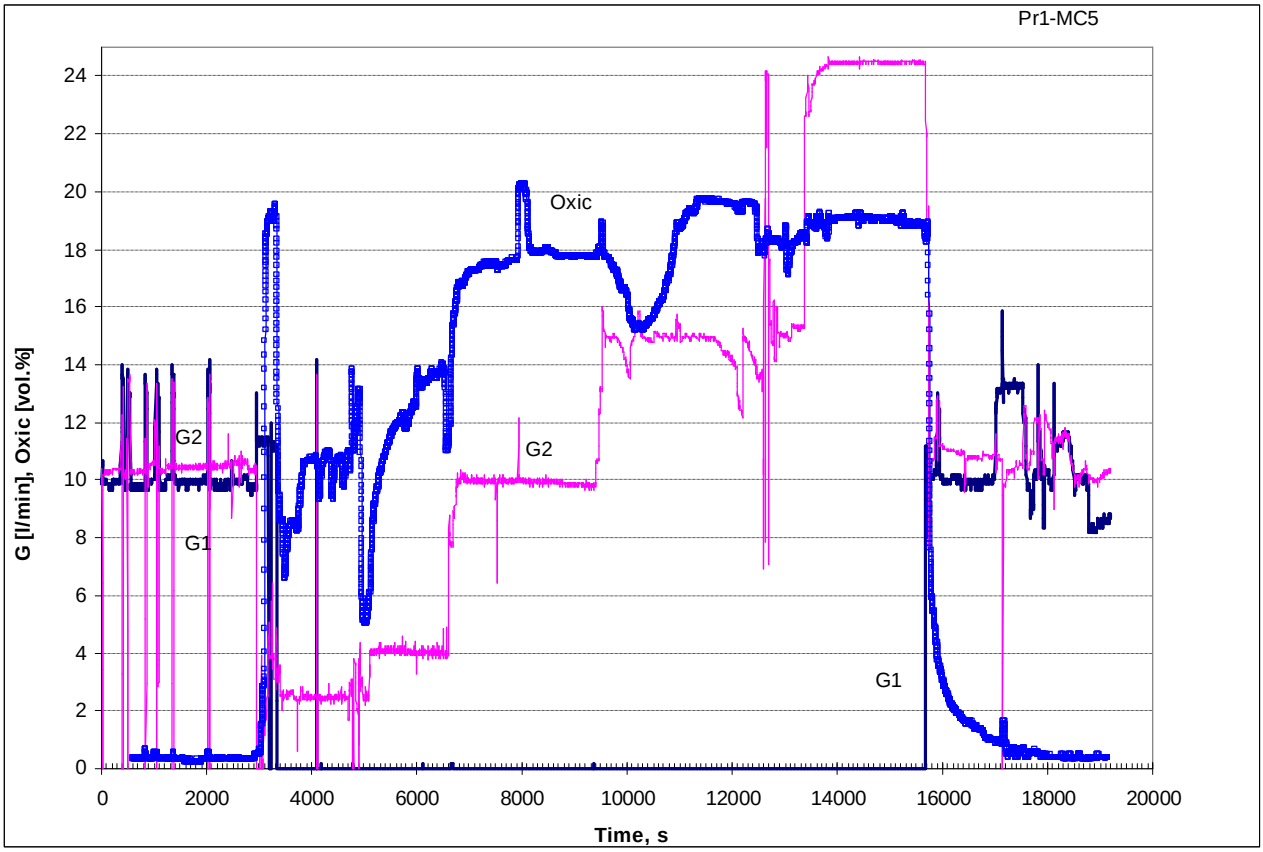

Fig. 5.Readings of oxygen sensor (O_{xic}), argon flowmeter G1 and air flowmeter G2

At 15,735 sec argon was supplied into the furnace and the readings of oxygen content in the gases removed from the furnace were monitored by the oxygen sensor (see Fig. 5). After the gas-melt system had achieved new equilibrium, the melt was sampled at 17123 sec for determining the oxygen-total metals ratio.

At 19,000 sec the HF heating was disconnected and the corium ingot was cooled down in argon.

3. Posttest analysis

3.1 Furnace disassembly

During the furnace disassembling, crusts and aerosol deposits were observed on the walls of crucible sections (Fig. 6). Thickness of the crust between the bottom calorimeter and corium ingot was approximately 0.5 mm. As soon as aerosols were collected from the crucible sections and ingot surface, the ingot was taken from the crucible after it had been carefully separated from the calorimeter. Fig.7 shows the bottom calorimeter surface after the test.

Fig. 6. Furnace appearance after the test

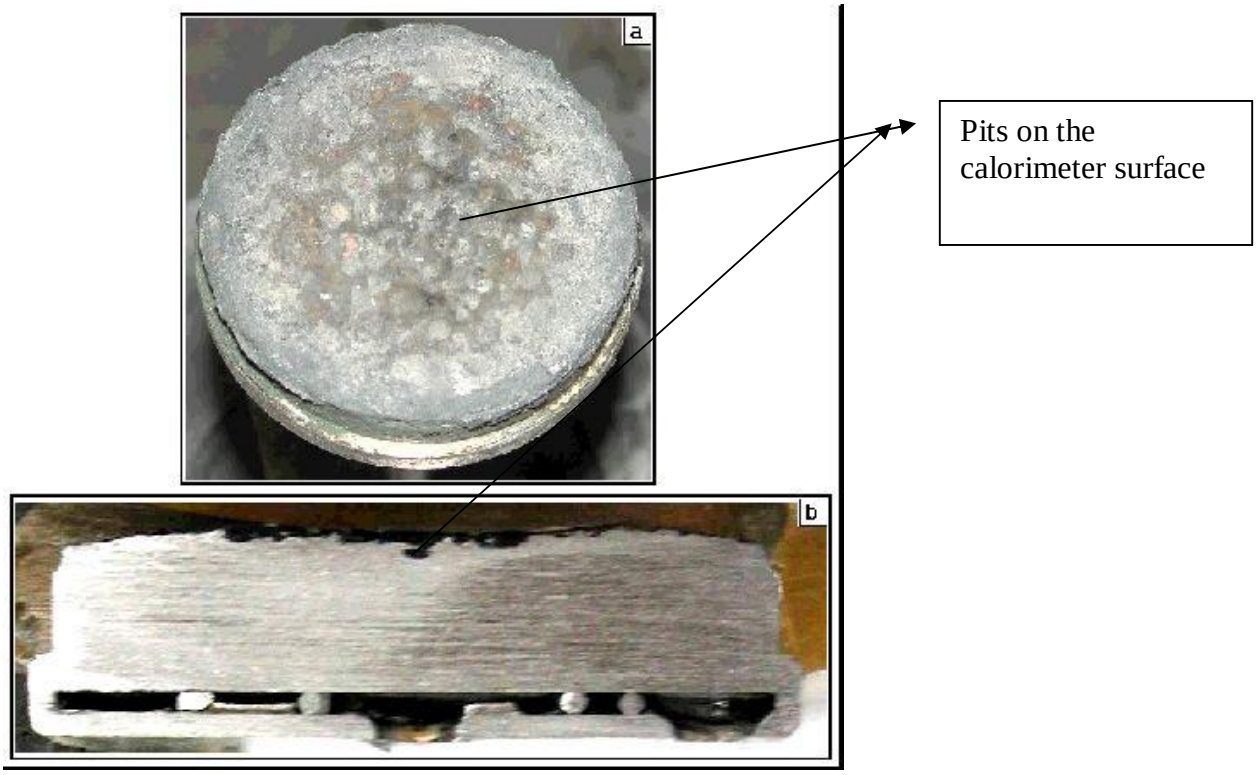

Fig. 7. Bottom water-cooled calorimeter made of stainless steel. Appearance after the test.

The pitted calorimeter surface confirms the interaction of molten corium and calorimeter steel.

3.2 Physico-chemical analysis

3.2.1 Initial components analysis

When preparing the test, the charge components (urania, zirconia and metallic zirconium) were checked for the main substance content. In addition, the powdered urania was checked by thermogravimetry and the oxygen/uranium ratio was found to equal 2.0. Table 1. shows the corium charge composition.

Table 1

Corium charge composition

Components	Main substance content, %	Impurities, %	Notes
UO_2 powder, dispersivity <200 μm	>99.0	Fe<0.03; As<0.0003; CuO<0.01; phosphates<0.002; chlorides<0.003.	Passport data, thermogravimetry
ZrO_2 powder, dispersivity <100 μm	(ZrO_2+HfO_2) >99.3	Al_2O_3<0.03; Fe_2O_3<0.05; CaO<0.03; MgO<0.02; SiO_2<0.2; TiO_2<0.1; P_2O_5<0.15; (Na_2O+K_2O)<0.02.	Passport data
Zr metallic	Zr/Nb-1% alloy >99.0	Nb<1.0	XRF results

3.2.2 The analysis of samples from products of melting

3.2.2.1 XRF analysis

The elemental analysis of the products of melting was made by the XRF spectrometry using the SPARK-1M/IBM PC spectrometer designed for the successive qualitative and quantitative determination of 66 chemical elements from Sc(21) to U(92) in a wide range of their concentrations in samples [2].

For this analysis, a special technique of compacted pellets was applied to the preparations. The two-layer pellets produced from a mixture of uranium, zirconium and iron oxides and fused in different proportions by the IMCC method served as calibration samples.

All the work on the samples preparation was carried out in argon. At first, the selected melt samples or ingot parts were crushed down to grains sized no more than 2 mm. Then an average sample was taken by quartering and milled into particles sized no more than 50 μm.

Three samples were taken during Pr1-MC5: the 1st one at the end of the 4th steady-state regime (13,314 sec), at the air flow rate of 15 l/min; the 2nd one – at the end of the 5th steady-state regime (15,000 sec), just before argon supply was switched on; and the 3rd one – before the furnace was shut down (17,123 sec).

Table. 2 presents the results of XRF analysis of the oxidic corium sampled during Pr1-MC5.

Table 2

Results of XRF analysis of the oxidic corium sampled during Pr1-MC5

Composition	Sample 1 (13,314 sec)	Sample 2 (15,000 sec)	Sample 3 (17,123 sec)
	mass %		
U	63.7	62.3	61.5
Zr	21.8	22.6	24.3
Fe	0.8	1.0	1.3
O*)	13.7	14.1	12.9

*) – oxygen was determined from the residue.

The presence of iron in the samples is explained by (1) the local interaction of molten corium and the bottom calorimeter (the pits on the calorimeter surface, 2.5 – 3.0 mm-deep, see Fig. 13) and the subsequent diffusion of iron ions into the melt, and (2) by partial interaction of molten corium with the steel probe during sampling.

3.2.2.2 Chemical analysis

The samples of molten corium taken during the test were analyzed for the content of U^{+4} and U^{+6} with the arsenazo III reagent [4]. The analysis was done using average samples taken by quartering and crushed to particles sized below 50 μm.

The technique of U^{+4} and U^{+6} determination with arsenazo III reagent is meant for the determination of uranium microquantities in corium samples with a sensitivity of 0.04 μg/ml The technique is based on the formation of stained compounds of uranium (IV) and arsenazo III in the 4 N HCl medium. Uranium is reduced by granulated zinc in the presence of ascorbic acid. At the interaction with arsenazo III, uranium (IV) yields a complex of green colour, while with the excessive reagent the observed colour is violet of different shades. Spectrophotometry is best with a 2 to 5-time higher molar content of the reagent. Staining occurs almost instantly and is stable for at least two hours. The technique allows determination of uranium (IV) and the total uranium in the solution. The quantity of uranium (VI) is calculated from the difference between the content of uranium (IV) and total uranium.

Free zirconium was determined in corium samples by the volumometric method [3] based on the measurement of the quantity of hydrogen released at the interaction of metallic zirconium, present in corium, with concentrated phosphoric acid. The reaction of metallic zirconium with concentrated phosphoric acid proceeds as follows:

(dissolution of free zirconium in phosphoric acid with production of two moles of hydrogen per each gram-atom of zirconium)

$$Zr + 4H_3PO_4 = Zr(H_2PO_4)_4 + 2H_2\uparrow. \quad (1)$$

The quantity of free zirconium is calculated proceeding from the volume of the released hydrogen using the formula given below:

$$Zr_{ce} = \frac{91{,}22 \cdot 273{,}15}{2 \cdot 22{,}416 \cdot 760} \cdot \left(\frac{V_2 \cdot P_2}{273{,}15 + t_2} - \frac{V_1 \cdot P_1}{273{,}15 + t_1} \right) \quad (2)$$

where

91,22 is the atomic weight of zirconium

273,15 is the absolute temperature of water freezing, K;

2241,60 is the volume of one mole of gaseous hydrogen at 273,15 K and 760 mm of mercury, l

V_2 and V_1 are gas volumes measured before and after the dissolution of the tested mixture, ml

P_2 and P_1 are the atmospheric pressure before and after the dissolution of the tested mixture, mm mercury

t_2 and t_1 are the ambient air temperature measured before and after the dissolution of the tested mixture, ^oC.

The determination of free and total zirconium makes it possible to evaluate the degree of zirconium oxidation (C_n) by the formula:

$$C_n = (Zr_{tot} - Zr_{fr.})/ Zr_{tot} * 100\%, \quad (3)$$

The results of chemical analysis of samples from the test are given in Tab. 3.

Table 3

Results of corium samples chemical analysis by different methods

Sample	Photocolorimetry (dissolution in H_2SO_4 and H_3PO_4)		ΣU	Volumometric method Zr^0 (fr.)
	U^{+4}	U^{+6}		
	Content, mass %			
1	65.41	not found	65.41	2.37±0.12
2	52.72	11.29	64.01	0
3	59.38	4.49	63.87	0
Large-area filters, in air	23.6	63.3	86.9	Was not determined
Large-area filters, in argon	33.3	53.3	86.6	Was not determined

From the U^{+6} / U^{+4} ratio in aerosols it was determined that stoichiometry of uranium oxides is close to U_3O_8. When air is supplied into the furnace, $(U,Zr)O_{2-x}$ is oxidized in the melt upper layers, thus leading to a more intense evaporation of melt components. It is predominantly UO_2 that evaporates from the melt and, presumably, undergoes further oxidation by atmospheric oxygen to U_3O_8. When argon is supplied into the furnace after the melt has oxidized, i.e. has

transformed to $(UZr)O_{2+x}$, the oxygen that starts evaporating from the melt together with UO_2 may also oxidize uranium oxide in its gas-aerosol phase to U_3O_8.

Table 4 summarizes inaccuracies of physico-chemical analyses.

Table 4

Inaccuracies of physico-chemical analyses

Element	Error % relat.	Method
U	5	XRF
Zr	10	XRF
Fe	10	XRF
U^{+4}	1	Photocolorimetry
Zr^0 (fr.)	10	Volumometric

3.2.3 Material balance for the test

To make the material balance for the test, the initial charge components and molten products were weighed to within 0.1 g. The material balance for the test is given in Tab. 5.

Table 5

Material balance for Pr1-MC5

Introduced into the melt, g		Collected after the test, g	
UO_2	1315.0	Ingot	1166.9
$UO_{2.24}$	53.7	Crusts on crucible sections	329.5
ZrO_2	162.0	Spillages	125.3
Zr	270.0	Liquid spillages	2.4
		Aerosols from sections	15.2
		Aerosols from flask	47.9
		Aerosols from medium-area filters	≈120.7
		Samples	62.3
		Corium from bottom calorimeter	≈20.0
∑	1800.7	∑	1890.2
Debalance	89.5		

According to the results of material balance, 183.8 g of U_3O_8 aerosols were collected during Pr1-MC5. Thus, approximately 176.8 g of UO_2 evaporated from the melt (see Tab. 3).

3.2.4 EDX analysis

The determination of the samples elemental composition was performed using the EDX analysis. The study employed the AVT-55 scanning electron microscope (Japan) with the Link_AN_10000/S85 microanalyzer attachment (Great Britain).

For each region of the template spectral characteristic was taken for determining its integral composition and that for each separated phase. The quantitative analysis was made by comparing spectral intensity of the reference (superpure, specially prepared substances) and studied samples. Uranium, Zr, Cr, Fe and Ni samples supplied together with the Link microanalyzer

were used as the standards. The quantity of oxygen was determined from the total intensity deficiency.

The threshold of reliable element determination depends on its sequential number in the Mendeleyev's periodic table and varies from 0.3 mass % for light elements to 0.1 mass % for heavy ones. The identification of smaller quantities of an element is unreliable. The content of oxygen was determined from the sample mass deficiency with an error not exceeding 4 mass %.

Table 6 contains EDX analysis the results of oxidic corium samples from the test.

Table 6

EDX analysis the results of oxidic corium samples from the test

Composition	Pr1-MC5		
	Sample 1	Sample 2	Sample 3
	mass %		
U	59.10	58.28	56.66
Zr	20.72	21.35	22.37
Fe	0.77	0.88	1.31
O	19.41	19.49	19.65

A higher oxygen content in samples than that determined by XRF analysis is due to samples afteroxidation during sections preparation.

3.2.5 Metallography

A view of the calorimeter surface after the test is given in Fig. 7. Upon completing the test, the calorimeter top was embedded in epoxy to avoid crumbling of a fragile oxidic film on the surface. Then it was cut along the axis. The metal surface microrelief was viewed and images of steel microstructure made with a metallographic microscope at magnifications varying from x50 to x300. The scale of the microstructure image was determined with a stage micrometer with a scale factor of 10 μm.

On the basis of measurements of the sample longitudinal macrosections and the obtained images, a curve of the specimen top microrelief evolution was plotted (see Curve 1 in Fig. 8).

The X-line shows the sample diameter, while the Y-line shows (top-down) the distances from the initial top surface of the calorimeter.

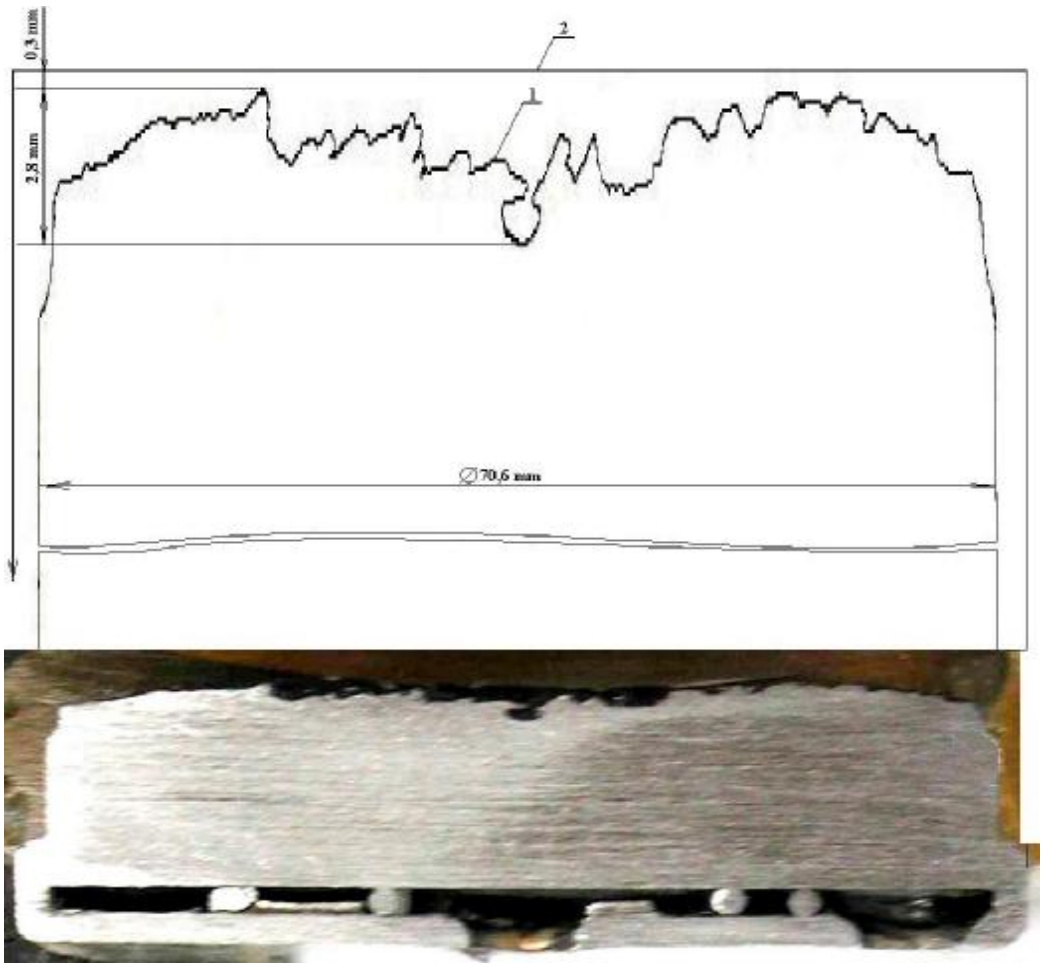

Fig. 8. Evolution of the top surface profile. Longitudinal section along the diameter, after interaction with corium.

2 and 1 – calorimeter surface position before and after interaction with corium.

The study of the surface condition and profile of the calorimeter longitudinal section yielded the following findings:

- The surface is uneven, covered with pits, which have a layer of iron and uranium oxides. The pits are 2.5 to 3.0 mm deep.
- Corrosion occurred not only on the top surface, but along the lateral surface as well.
- The depth of metal layer with the signs of chemical impact varies from 0.3 to 3.1 mm.
- The depth of the thermal impact layer with changed grain size is 8 mm

The microstructure of the subsurface layers and of the calorimeter axial section are shown in Fig. 9. Three characteristic layers may be distinguished in the thermal impact zone.

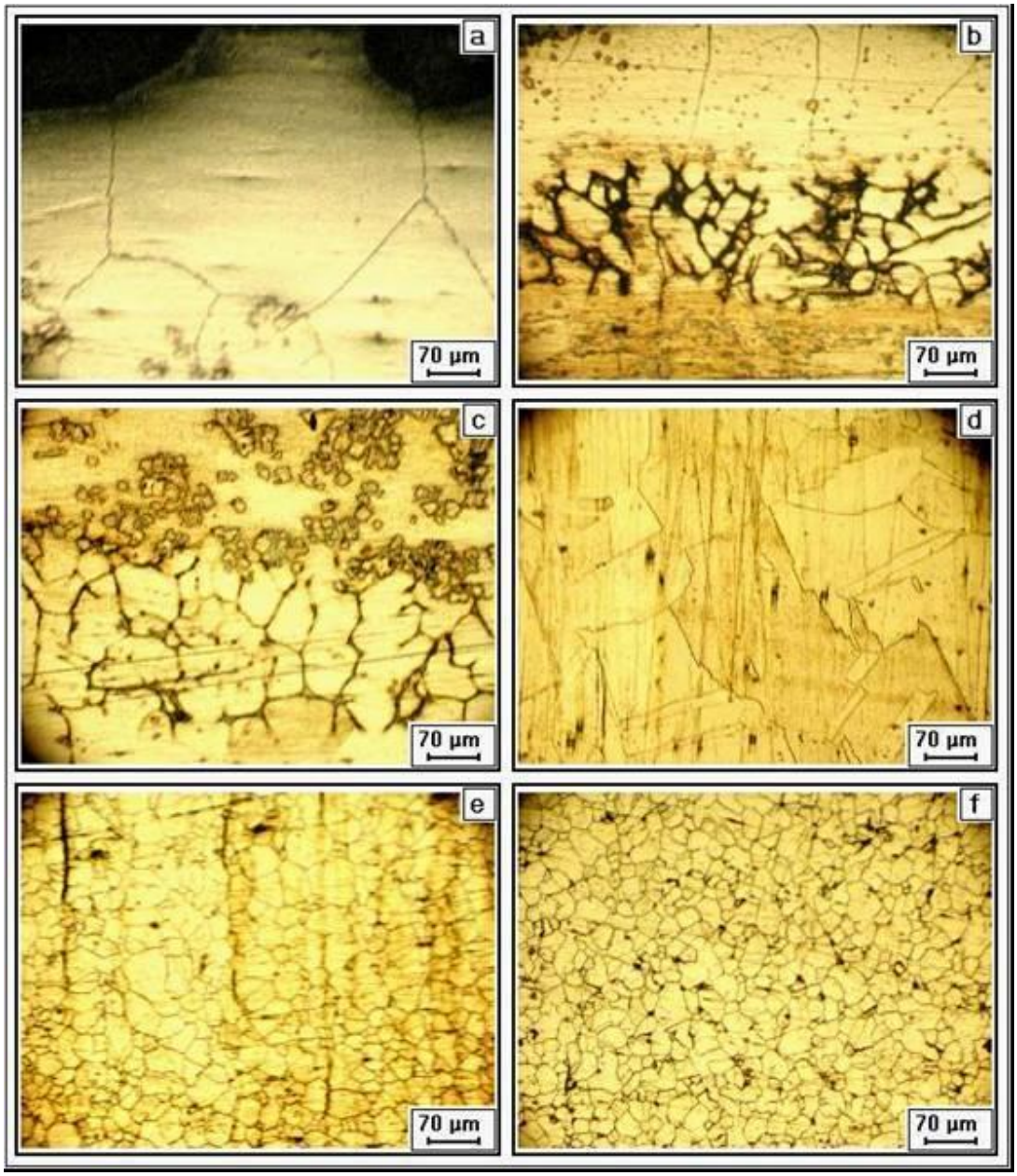

Fig. 9. Microstructure image

1) The microstructure of the steel upper layer (Fig. 9a) may be identified as decarbonized ferritic, with very large grain, located at a depth up to 1 mm. Such a microstructure formed as a result of long-term exposure of the sample top at a temperature close to that of melting and further transformation of austenite into ferrite at a high temperature. Regions with aggregations of numerous small grains were found in this layer at a depth of approximately 1 mm (see Fig. 9c). It should be noted that cracks and pores were observed in said regions (Fig. 10e).

2) The second layer extends to the depth of 2 mm; its structure is shown in Fig. 9b,c. The redistribution of carbon and alloying elements along grain boundaries may be observed in this layer, which is related to diffusion occurring under gradient conditions.

3) The third layer has a coarse-grain austenitic structure and extends to the depth of 7 mm (see Fig. 9d), while at about 8 mm a smooth transit to a fine-grain structure occurs (see Fig.9e).

Still deeper (Fig. 9f), there was a layer with grain size comparable to the initial.

Fig. 10 shows images of the steel subsurface layers along the sample longitudinal section. The pits from local steel corrosion may be observed.

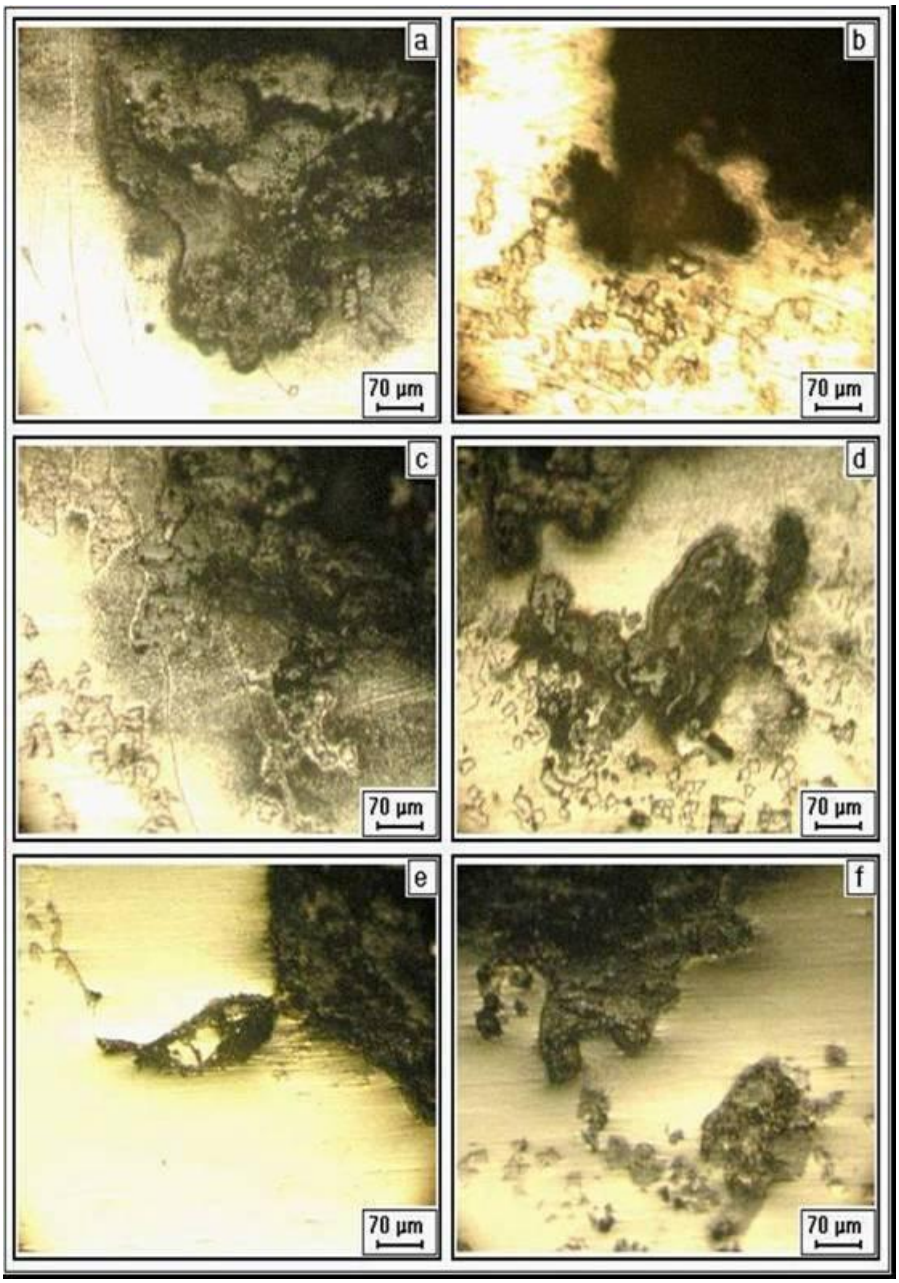

Fig. 10. Image of fragments of local corrosion pits

The physico-chemical analyses results lead to the following conclusions:

- The debalance of 89.5 g from the test melting in air is mainly due to the oxidation of free zirconium available in the melt. According to the reaction $Zr + O_2 = ZrO_2$, at full oxidation of total zirconium, the mass of corium had to gain 94.7 g. A smaller value (see Tab. 5) is determined by the losses of a part of aerosols at opening the furnace, as well as by the crusts on crucible sections, which contained zirconium, which might not fully oxidize during the test.
- The full zirconium oxidation in the melt has most likely occurred in the beginning of the 5^{th} period of stabilized temperature, as by the end of the 4^{th} period 2.4% Zr had not oxidized, while in the end of the 5^{th} period the concentration of U^{+6} in the melt was 11.3% thus indicating to the excess of oxygen in corium, if compared to the stoichiometric composition.

- Intense interaction of the melt with calorimeter steel has been noted. The maximum depth of ablation amounted to ~3 mm. It was impossible to determine the oxygen potential at which steel ablation occurred in this test

4. Corium oxidation

4.1. Initial experimental data on the oxidation kinetics

Table 7

Recalculation of charge into stoichiometric oxides (allowing for $UO_{2.24}$)

Introduced into melt	**UO_2**	**ZrO_2**	**Zr**
g	1367.95	164.9	267.85
mass %	75.97	9.16	14.87
mol	5.07	1.34	2.94
mol %	54.24	14.33	31.44

According to the material balance data (see Tabs. 5 and 7), the equilibrium involved ~1166.9+62.3+(120.7+47.9+15.2-6.98 (aerosols minus oxygen for afteroxidation of uranium))-89.5=1316.52 g of the melt, i.e. 73.11% of the charge mass. Thus, in the first approximation, the mass of free zirconium in the melt before the supply of oxygen amounted to ~195.83 g (73.11% of 267.85 g), while the mass of oxygen-bound zirconium was 89.25 g. Therefore, the corresponding index of corium is C-31.31.

After the molten pool preparation, at 2,960 sec the inert atmosphere was replaced with air fed at a flow rate of 2.5 l/min. At 5,280 sec the flow rate was increased to 4 l/min. At 6,940 sec, the flow rate was increased to 10 l/min, and at 9,720 sec – up to 15 l/min. At 13,720 the flow rate was increased to 24.4 l/min, and at 15,735 sec argon was supplied into the furnace. Curves from the test are given in Fig. 11. Table 8 presents the recalculated exposure time and air flow rates for each period.

Table 8

Exposure time and air flow rate

Period No.	**$t_{begin.}$, c**	**t_{end}, c**	**Duration** Dt		**Air flow rate, l/sec**
			sec	**h**	
1	3180	4782	1,602	0.45	0.04
2	4782	6538	1,756	0.49	0.07
3	6538	9546	3,008	0.84	0.17
4	9546	13437	3,891	1.08	0.25
5	13437	15735	2,298	0.64	0.41

According to the material balance data, 176.82 g UO_2, evaporated from the melt during the test and were afteroxidized to U_3O_8 by 6.98 g oxygen. Formation of aerosols was observed at the beginning of each period, so (in the absence of quantitative data on the amount of aerosols released during each period), in order to account for the aerosols oxidation, 1.4 g of oxygen per each period should be deduced from the calculated mass of the oxygen used for zirconium oxidation.

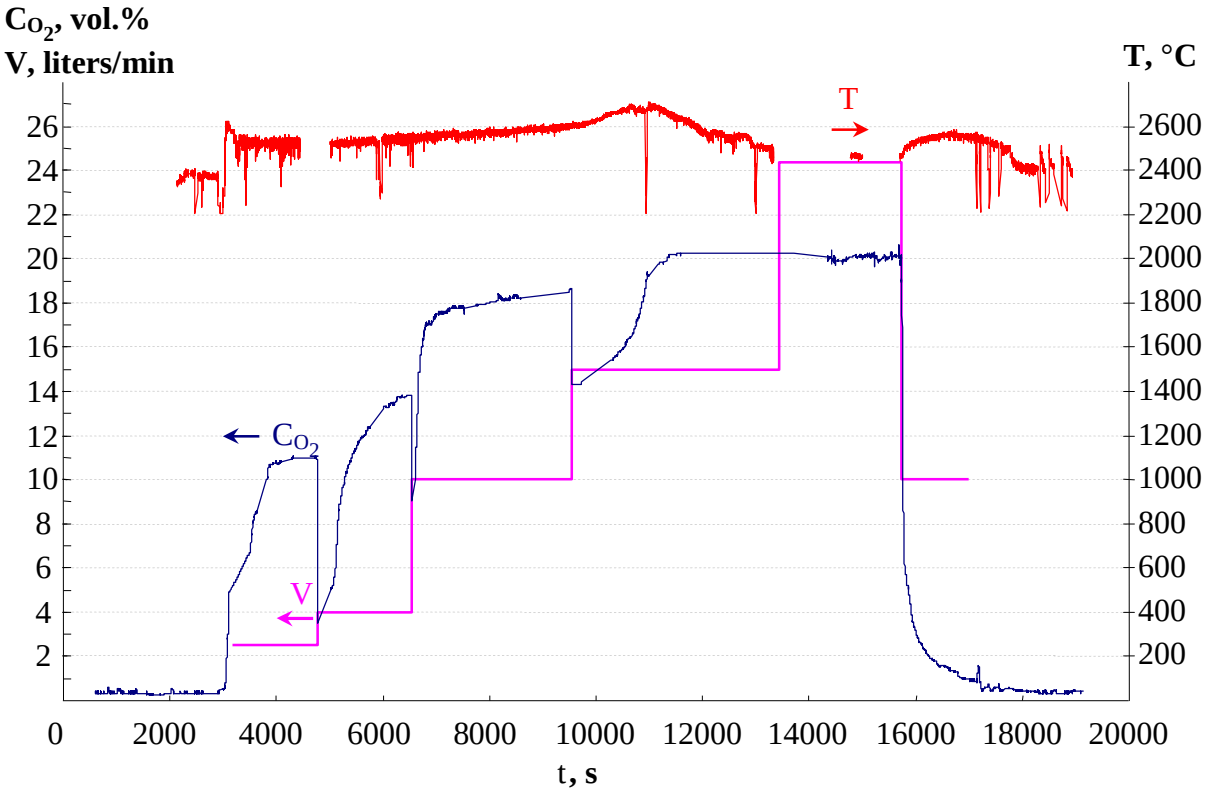

Fig. 11. Evolution of oxygen concentration at the furnace outlet, vol. % (——), air flow rate, l/min (——) – melt surface temperature (——).

4.2. Experimental data processing

Data processing for the first period:

1. Processing of the data for the period from 3,180 sec to 4,782 sec (without distinguishing between two mechanisms of oxidation)(The 1st mechanism is the non-stationary "rapid" oxidation, and the 2nd one is the quasistationary "slow" oxidation).

The evolution of the oxygen concentration ($C_{O_2}(\tau)$ in Fig. 11) is preliminarily presented as a piecewise-linear interpolation with identical intervals ($C_{O_2}(\tau)$ in Fig. 12). Then the oxygen absorption during this period is calculated from the following relation (see $m_{O_2}(\tau)$ in Fig.12):

$$m_{O_2}(\tau) = \int_{\tau_0}^{\tau} \frac{V}{V_M} M_{O_2} \frac{C^0_{O_2} - C_{O_2}(\tau)}{100} d\tau, \text{ g}, \qquad (4)$$

where τ_0 is the beginning of given period, sec; V is the air flow rate, l/sec; V_M=22.4 is the volume of 1 mole of gas, l/mol; M_{O_2}=31.9998 is the molecular mass of oxygen, g/mol; $C^0_{O_2}$ =20.25 is the concentration of oxygen in air (oxygen sensor averaged readings from the last half of the 4th period and 5th period), vol.%; $C_{O_2}(\tau)$ is the function of oxygen concentration in gas at the furnace outlet, vol.%.

The relation $m_{O_2}(\tau)$ can be approximated by the function

$m`_{O_2}(\tau) = 87.685 - \frac{7.332 \cdot 10^5}{\tau} + \frac{2.341 \cdot 10^9}{\tau^2} - \frac{2.849 \cdot 10^{12}}{\tau^3}$ with a third-degree inverse polynomial.

After differentiating the function $m`_{O_2}(\tau)$, the evolution of the oxygen absorption rate was determined: $\upsilon_{O_2}(\tau) = \frac{\partial m`_{O_2}(\tau)}{\partial \tau} = \frac{7.332 \cdot 10^5}{\tau^2} - \frac{4.681 \cdot 10^9}{\tau^3} + \frac{8.548 \cdot 10^{12}}{\tau^4}$, g/sec.

To verify the validity of the approximations, the rate of the oxygen absorbtion was obtained by numerical integration with the trapezium quadrature formula:

$$\upsilon`_{O_2}(\tau) \approx \int_a^b S(x)dx = \sum_{i=1}^{n} n \frac{y_{i-1} + y_i}{2}, \qquad (5)$$

where $S(x)$ is the piecewise continuous function, n is the function pitch.

Then, $C`_{O_2}(\tau)$ is calculated by the formula:

$$C`_{O_2}(t)m_{O_2}(t) = -\frac{\int_{t_o}^{t}\left[u_{O_2}(t) - \frac{V}{V_m} M_{O_2} \frac{C^0_{O_2}}{100}\right]dt}{\int_{t_o}^{t} \frac{V}{V_M} M_{O_2} \frac{1}{100} dt} \qquad (6)$$

Finally, $C`_{O_2}(\tau) = 83.129 - \frac{9.787 \cdot 10^5}{\tau} + \frac{4.492 \cdot 10^9}{\tau^2} - \frac{6.957 \cdot 10^{12}}{\tau^3}$.

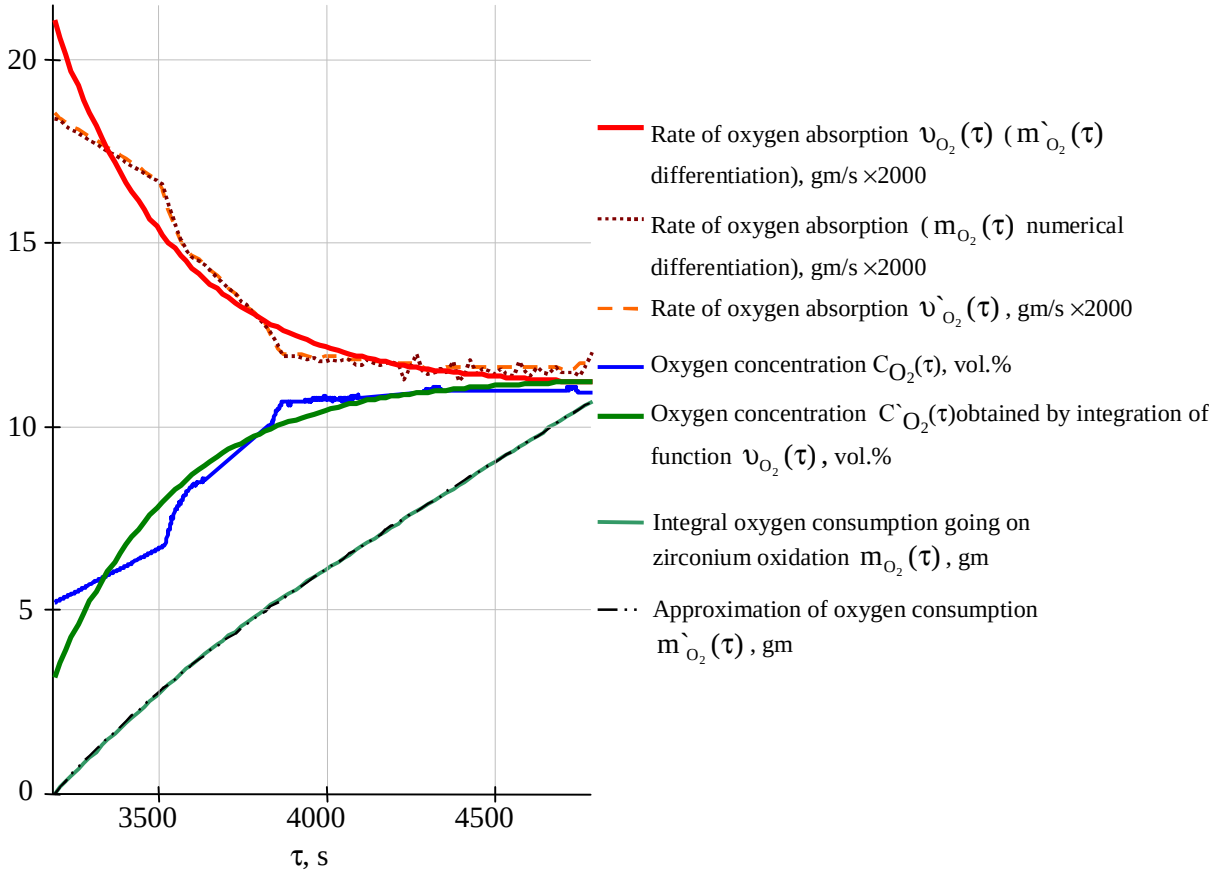

Fig. 12. Calculation of the absorbed oxygen quantity and of the absorption rate

The calculated result of the oxygen quantity absorbed during the first period, obtained by means of the adaptive integration method, which facilitates integration in cases with rapidly changing functions (MathCAD package), is 10.6803 g. The application of the Romberg's method yields 10.6835 g. According to the trapezium rule, the quantity equals 10.7847 g of oxygen. 10.6893 g were obtained by integrating the smoothed absorption rate. Therefore, 10.6844±0.005 g of oxygen were absorbed during the first period. Thus, the integration error is negligibly small in comparison with the error of measuring the oxygen partial pressure. It should be noted, that due to the impossibility of accounting the oxygen used for aerosols oxidation, an assumption was made that equal amounts of aerosols were oxidized during each period, i.e., of 10.68 g of oxygen absorbed during the 1st period, 1.4 g were spent on the aerosols afteroxidation from UO_2 to presumably U_3O_8.

2. Processing of the data for the period from 3,180 sec to 4,782 sec (approximation, taking into account two mechanisms of oxidation)

In the evolution of the oxygen concentration ($C_{O_2}(\tau)$ in Fig. 11, 12), two periods may be identified, one of which corresponds to the regime of relatively rapid oxygen absorption (before 3,850 sec) and the other – to the regime of relatively slow oxygen absorption (starting from 3910 sec).

For the interval that corresponds to rapid oxygen absorption, $C_{O_2}(\tau)$ is approximated by the function $C`_{O_2}(\tau) = 801.976\text{-}0.683\tau + 1.93\cdot10^{-4}\tau^2 - 1.791\cdot10^{-8}\tau^3$ using a third-degree polynomial, while for the interval corresponding to slow oxygen absorption – by the function $C`_{O_2}(\tau) = 2.622 + \frac{82832.91}{\tau} - \frac{2.227\cdot10^{8}}{\tau^2} + \frac{8.466\cdot10^{10}}{\tau^3}$ with the reverse third-degree polynomial.

On the basis of the approximating relations $C`_{O_2}(\tau)$ obtained according to (4), the oxygen balance was calculated, as well as the oxygen absorption rate during the regime of rapid oxygen absorption $\upsilon_{O_2}(\tau) = -.465\text{+}4.067\cdot10^{-4}\tau - 1.149\cdot10^{-7}\tau^2 + 1.066\cdot10^{-11}\tau^3$, and during the regime of slow oxygen absorption $\upsilon_{O_2}(\tau) = 1.073\cdot10^{-2} - \frac{49.303}{\tau} + \frac{1.325\cdot10^{5}}{\tau^2} - \frac{5.039\cdot10^{7}}{\tau^3}$.

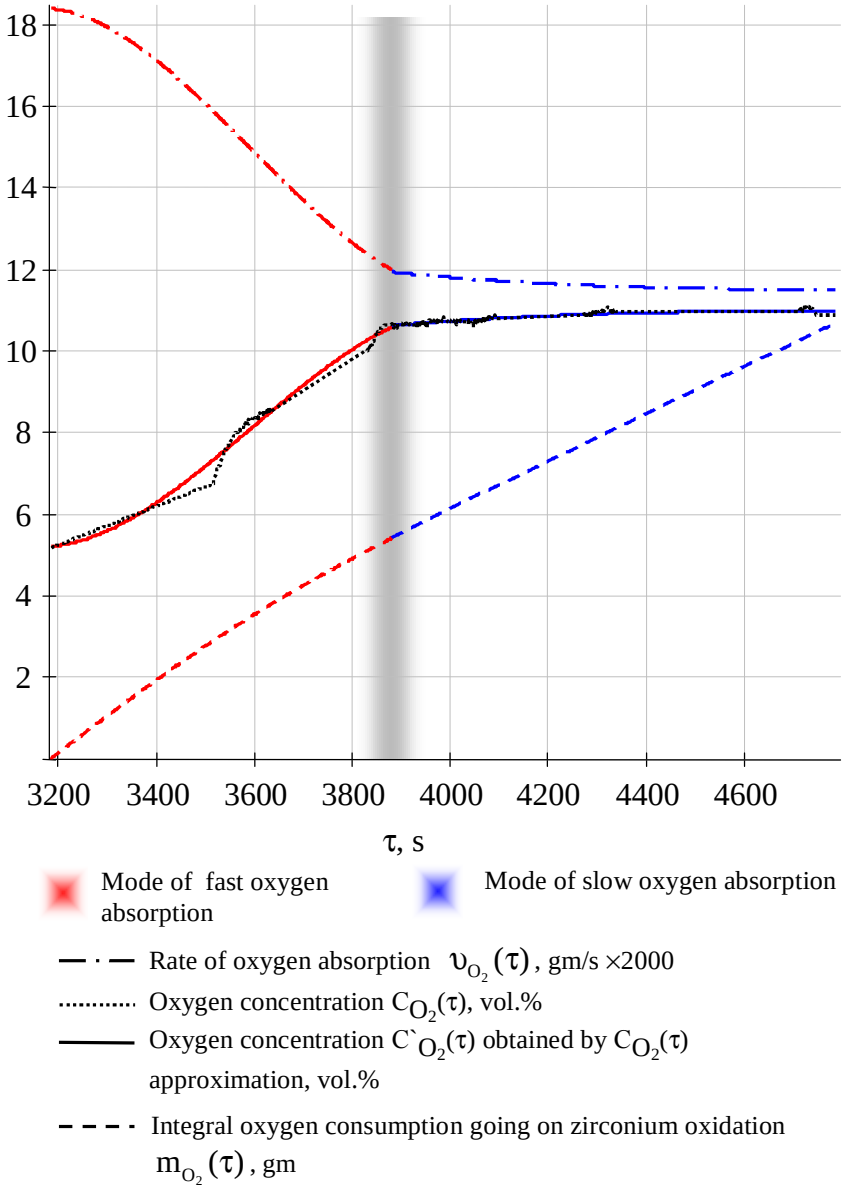

Fig. 13. Calculation of the oxygen absorption rate, assuming two mechanisms

Data processing for the second period:

1. Processing of the data for the period from 4,782 sec to 6,538 sec (without distinguishing between two mechanisms of oxidation)
By applying the algorithm, described in the section on data processing for the 1st period, the following relations were obtained:

- for oxygen absorption: $m`_{O_2}(\tau) = 236.972 - \frac{3.469\cdot 10^6}{\tau} + \frac{1.896\cdot 10^{10}}{\tau^2} - \frac{3.726\cdot 10^{13}}{\tau^3}$.

- for the oxygen absorption rate: $\upsilon_{O_2}(\tau) = \frac{3.469\cdot 10^6}{\tau^2} - \frac{3.792\cdot 10^{10}}{\tau^3} + \frac{1.118\cdot 10^{14}}{\tau^4}$.

- for the oxygen concentration: $C`_{O_2}(\tau) = 139.828 - \frac{2.675\cdot 10^6}{\tau} + \frac{1.882\cdot 10^{10}}{\tau^2} - \frac{4.399\cdot 10^{12}}{\tau^3}$.

The quantity of oxygen absorbed during the 2nd period, calculated applying the adaptive method, was 16.6059 g, 16.6015 g when the Romberg's method was applied, 16.664 g if calculated using the trapezium rule, and 16.697 g by integrating the approximation of the absorption rate. Therefore, 16.642±0.05 g of oxygen were absorbed during the 2nd period, of which 1.4 g were used for the urania aerosols afteroxidation.

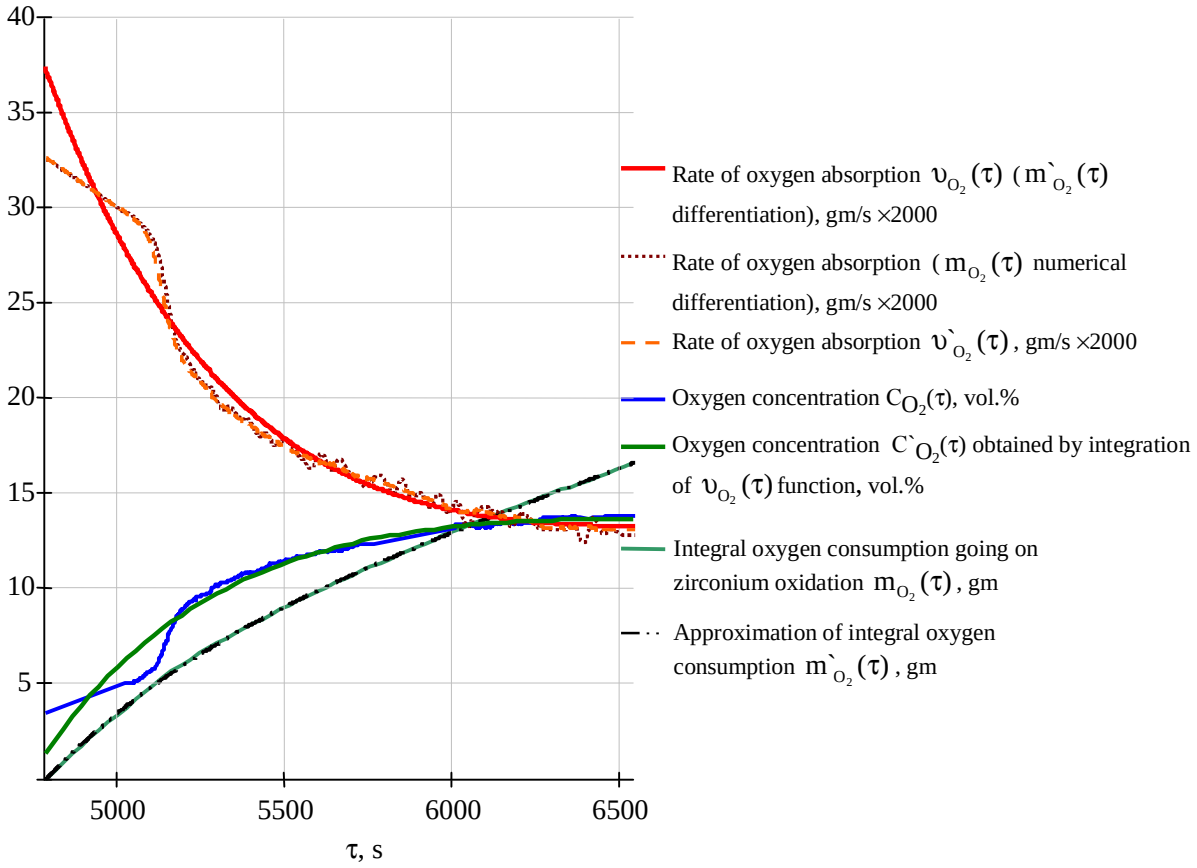

Fig. 14. Calculation of the absorbed oxygen quantity and of the absorption rate

2. Processing of the data for the period from 4,782 sec to 6,538 sec (approximation, taking into account two mechanisms of oxidation)

The approximating relation for the oxygen concentration during the regime of rapid absorption:

$$C`_{O_2}(\tau) = \frac{1}{-14.464+6.273\cdot10^{-3}\tau-6.676\cdot10^{-7}\tau^2}$$ and that for the regime of slow absorption:

$$C`_{O_2}(\tau) = -38.25+\frac{6.71\cdot10^{5}}{\tau}-\frac{2.004\cdot10^{9}}{\tau^2}-\frac{1.021\cdot10^{12}}{\tau^3}.$$

The oxygen absorption rate during the regime of rapid oxygen absorption:

$$\upsilon_{O_2}(\tau) = 1.967\cdot10^{-2}-\frac{1}{-1.519\cdot10^{4}+6.587\tau-7.01\cdot10^{-4}\tau^2}$$ and that for the regime of slow absorption: $$\upsilon_{O_2}(\tau) = 5.609\cdot10^{-2}-\frac{639.003}{\tau}+\frac{1.908\cdot10^{6}}{\tau^2}-\frac{9.722\cdot10^{8}}{\tau^3}.$$

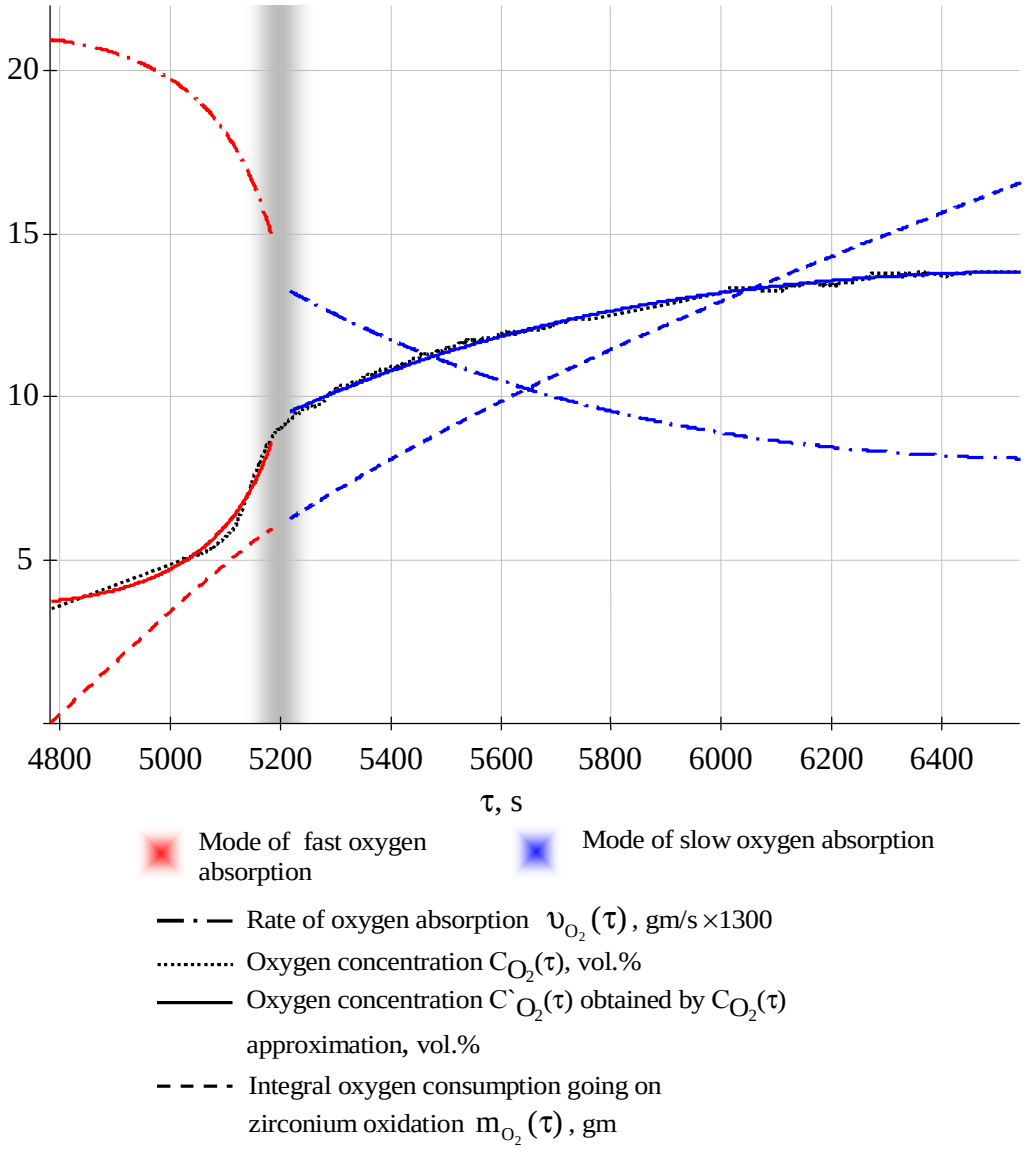

Fig. 15. Calculation of the oxygen absorption rate, assuming two mechanisms

Data processing for the third period:

1. Processing of the data for the period from 6,538 sec to 9,546 sec (without distinguishing between two mechanisms of oxidation)

By applying the algorithm, described in the section on data processing for the 1st period, the following relations were obtained:

- for the oxygen absorption:

$$m`_{O_2}(\tau) = -6.306\cdot10^{6} + 538.462\tau - 0.197\tau^{2} + 3.978\cdot10^{-5}\tau^{3} - 4.817\cdot10^{-9}\tau^{4} + \ldots$$
$$+3.493\cdot10^{-13}\tau^{5} - 1.403\cdot10^{-17}\tau^{6} + 2.412\cdot10^{-22}\tau^{7}$$

- for the oxygen absorption rate:

$$\upsilon_{O_2}(\tau) = 538.462 - 0.393\tau + 1.193\cdot10^{-4}\tau^{2} - 1.927\cdot10^{-8}\tau^{3} + \ldots$$
$$+1.746\cdot10^{-12}\tau^{4} - 8.421\cdot10^{-17}\tau^{5} + 1.688\cdot10^{-21}\tau^{6}$$

- for the oxygen concentration:

$$C`_{O_2}(\tau) = -2.209\cdot10^{5} + 161.958\tau - 0.049\tau^{2} + 8\cdot10^{-6}\tau^{3} - \ldots$$
$$-7.278\cdot10^{-10}\tau^{4} + 3.523\cdot10^{-14}\tau^{5} - 7.09\cdot10^{-19}\tau^{6}$$

The quantity of oxygen absorbed during the 3rd period, calculated applying the adaptive method, was 21.7272 g, 21.742 g when the Romberg's method was applied, 21.8196 g if calculated using the trapezium rule, and 21.723 g by integrating the approximation of the absorption rate.

Therefore, 21.753±0.05 g of oxygen were absorbed during the 3rd period, of which 1.4 g were used for the urania aerosols afteroxidation.

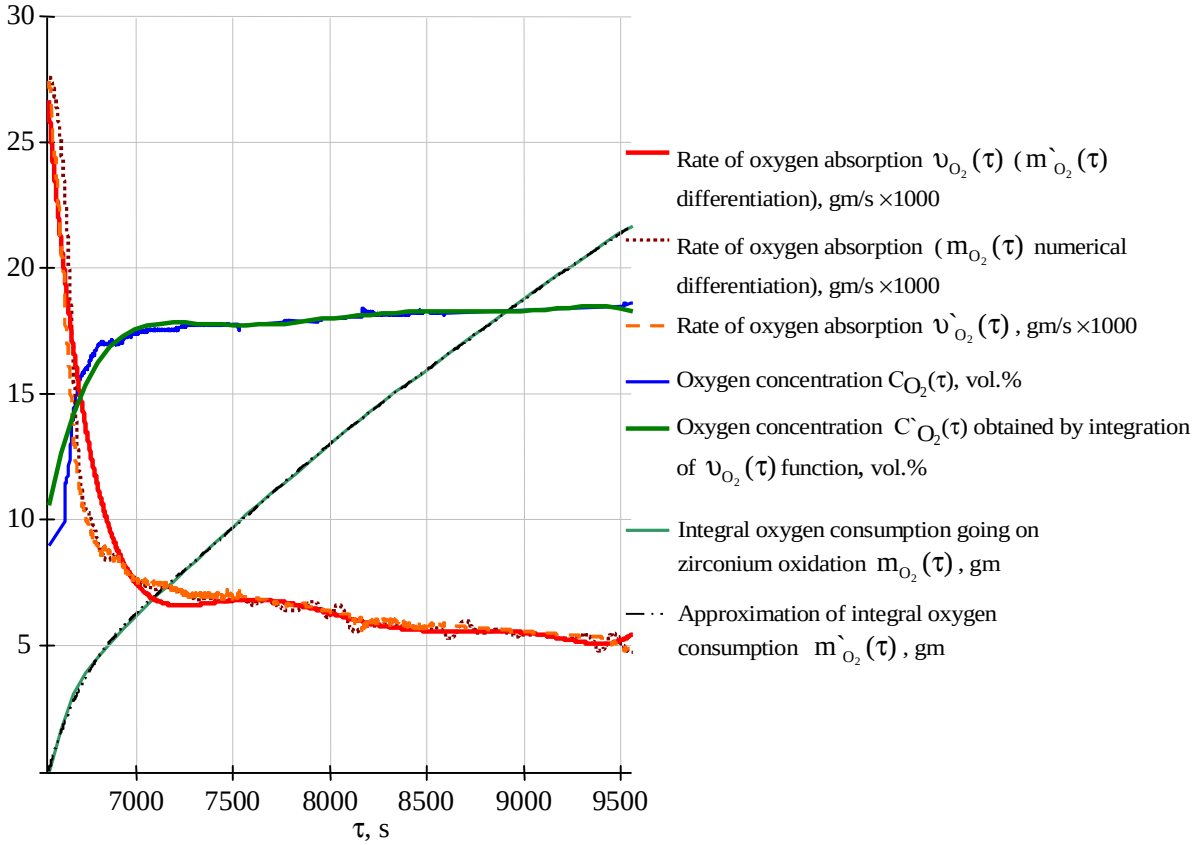

Рис. 16. Calculation of the absorbed oxygen quantity and of the absorption rate

2. Processing of the data for the period from 6,538 sec to 9,546 sec (approximation, taking into account two mechanisms of oxidation)

The approximating relation for the oxygen concentration during the regime of rapid oxygen absorption: $C`_{O_2}(\tau) = -3.718\cdot10^{5} + \frac{7.422\cdot10^{9}}{\tau} - \frac{4.938\cdot10^{13}}{\tau^2} + \frac{1.095\cdot10^{17}}{\tau^3}$, during the transitional period: $C`_{O_2}(\tau) = 1.372\cdot10^{4} - \frac{2.901\cdot10^{8}}{\tau} + \frac{2.046\cdot10^{12}}{\tau^2} - \frac{4.811\cdot10^{15}}{\tau^3}$ and during the regime of slow absorption: $C`_{O_2}(\tau) = 12.734 + \frac{1.451\cdot10^{5}}{\tau} - \frac{1.08\cdot10^{9}}{\tau^2} + \frac{2.072\cdot10^{12}}{\tau^3}$.

The oxygen absorption rate during the regime of rapid oxygen absorption:

$\upsilon_{O_2}(\tau) = 885.3 - \frac{1.767\cdot10^{7}}{\tau} + \frac{1.176\cdot10^{12}}{\tau^2} - \frac{2.607\cdot10^{14}}{\tau^3}$, during the transitional period:

$\upsilon_{O_2}(\tau) = -32.6 + \frac{6.907\cdot10^{5}}{\tau} - \frac{4.872\cdot10^{9}}{\tau^2} + \frac{1.145\cdot10^{13}}{\tau^3}$ and during the regime of slow absorption:

$\upsilon_{O_2}(\tau) = 1.886\cdot10^{-2} - \frac{345.5}{\tau} + \frac{2.571\cdot10^{6}}{\tau^2} - \frac{4.933\cdot10^{10}}{\tau^3}$.

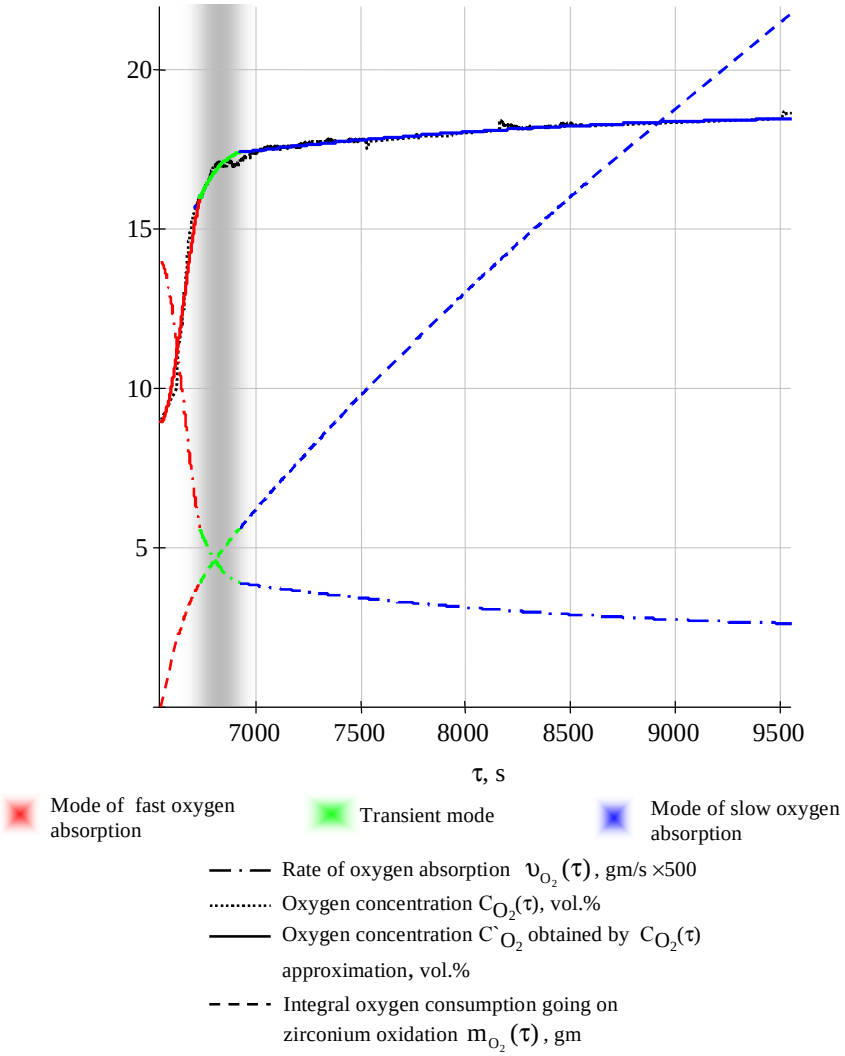

Fig. 17. Calculation of the oxygen absorption rate, assuming two mechanisms

Data processing for the fourth period:

1. Processing of the data for the period from 9,546 sec to 13,437 sec (without distinguishing between two mechanisms of oxidation)
By applying the algorithm, described in the section on data processing for the 1st period, the following relations were obtained:
- for the oxygen absorption:

$$m`_{O_2}(\tau) = -6.306\cdot10^{6} + 538.462\tau - 0.197\tau^{2} + 3.978\cdot10^{-5}\tau^{3} - 4.817\cdot10^{-9}\tau^{4} + \ldots$$
$$+3.493\cdot10^{-13}\tau^{5} - 1.403\cdot10^{-17}\tau^{6} + 2.412\cdot10^{-22}\tau^{7}$$

- for the oxygen absorption rate:

$$\upsilon_{O_2}(\tau) = 538.462 - 0.393\tau + 1.193\cdot10^{-4}\tau^{2} - 1.927\cdot10^{-8}\tau^{3} + \ldots$$
$$+1.746\cdot10^{-12}\tau^{4} - 8.421\cdot10^{-17}\tau^{5} + 1.688\cdot10^{-21}\tau^{6}$$

- for the oxygen concentration:

$$C`_{O_2}(\tau) = -2.209\cdot10^{5} + 161.958\tau - 0.049\tau^{2} + 8\cdot10^{-6}\tau^{3} - \ldots$$
$$-7.278\cdot10^{-10}\tau^{4} + 3.523\cdot10^{-14}\tau^{5} - 7.09\cdot10^{-19}\tau^{6}$$

The quantity of oxygen absorbed during the 4th period calculated applying the adaptive method was 24.01 g, 24.009 g when the Romberg's method was applied, 24.01 g if calculated using the trapezium rule, and 23.93 g by integrating the approximation of the absorption rate. The oxygen absorption stopped at 11,579 sec.

Therefore, 24.01 g of oxygen were absorbed during the 4th period, of which 1.4 g were used for the urania aerosols afteroxidation.

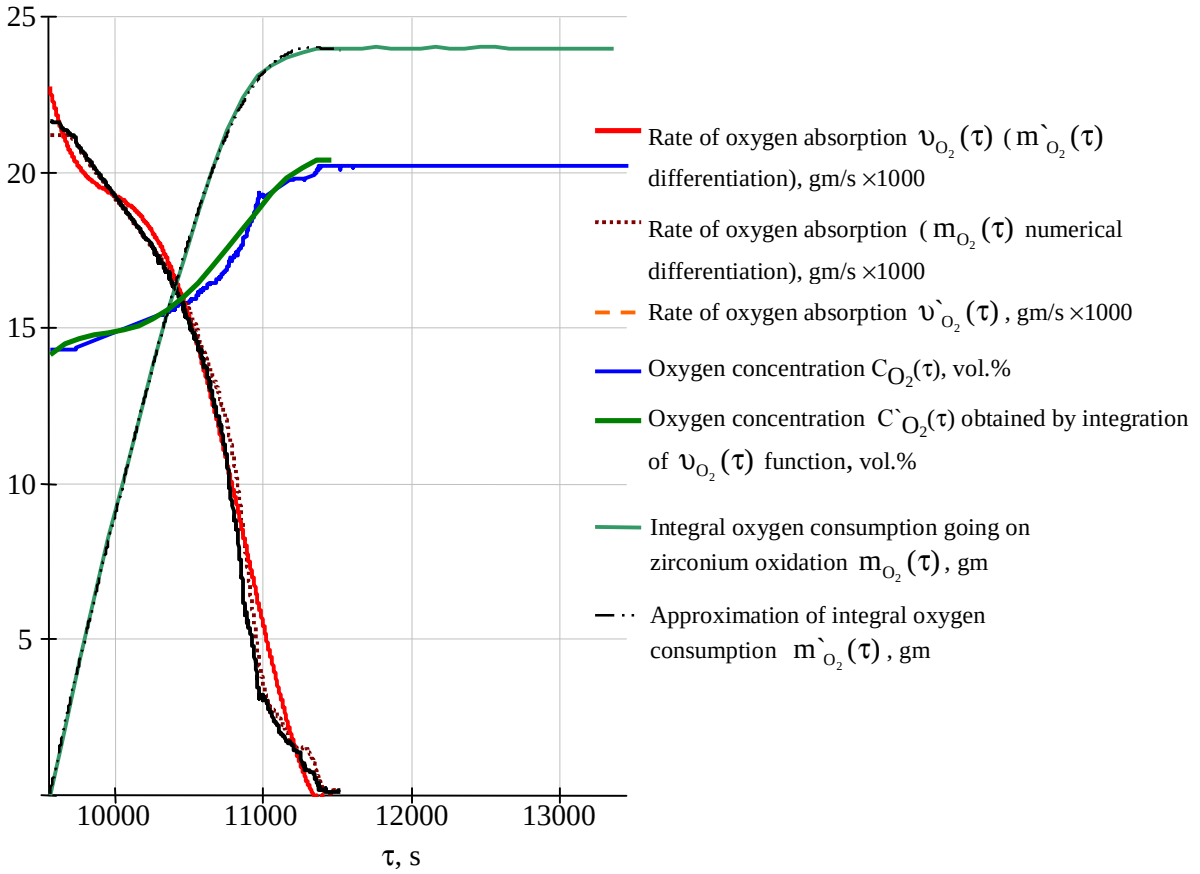

Fig. 18. Calculation of the absorbed oxygen quantity and of the absorption rate

2. Processing of the data for the period from 9,546 sec to 13,437 sec (approximation, taking into account two mechanisms of oxidation)

The approximating relation for the oxygen concentration during the regime of rapid oxygen absorption:

$C`_{O_2}(\tau) = -5.569\cdot10^{5} + 276.866\tau - 0.055\tau^{2} + 5.467\cdot10^{-6}\tau^{3} - 2.714\cdot10^{-10}\tau^{4} + 5.388\cdot10^{-15}\tau^{5}$, during the transitional period: $C`_{O_2}(\tau) = -1.491\cdot10^{4} + \frac{7.271\cdot10^{8}}{\tau} - \frac{1.327\cdot10^{13}}{\tau^{2}} + \frac{1.075\cdot10^{17}}{\tau^{3}} - \frac{3.264\cdot10^{20}}{\tau^{4}}$ and during the regime of slow absorption the concentration of oxygen at the outlet equals the oxygen concentration in air (taking into account the error of determining the oxygen partial pressure by the oxygen sensor) $C`_{O_2}(\tau) = 20.25$.

The oxygen absorption rate during the regime of rapid oxygen absorption:

$\upsilon_{O_2}(\tau) = 53.32 - \frac{2.596\cdot10^{6}}{\tau} + \frac{4.739\cdot10^{10}}{\tau^{2}} - \frac{3.839\cdot10^{14}}{\tau^{3}} + \frac{1.166\cdot10^{18}}{\tau^{4}}$, during the transitional period: $\upsilon_{O_2}(\tau) = 1.989\cdot10^{3} - 6.989\tau + 1.965\cdot10^{-4}\tau^{2} - 1.952\cdot10^{-6}\tau^{3} + 9.692\cdot10^{-11}\tau^{4}$ and during the regime of slow absorption: $\upsilon_{O_2}(\tau) = 0$.

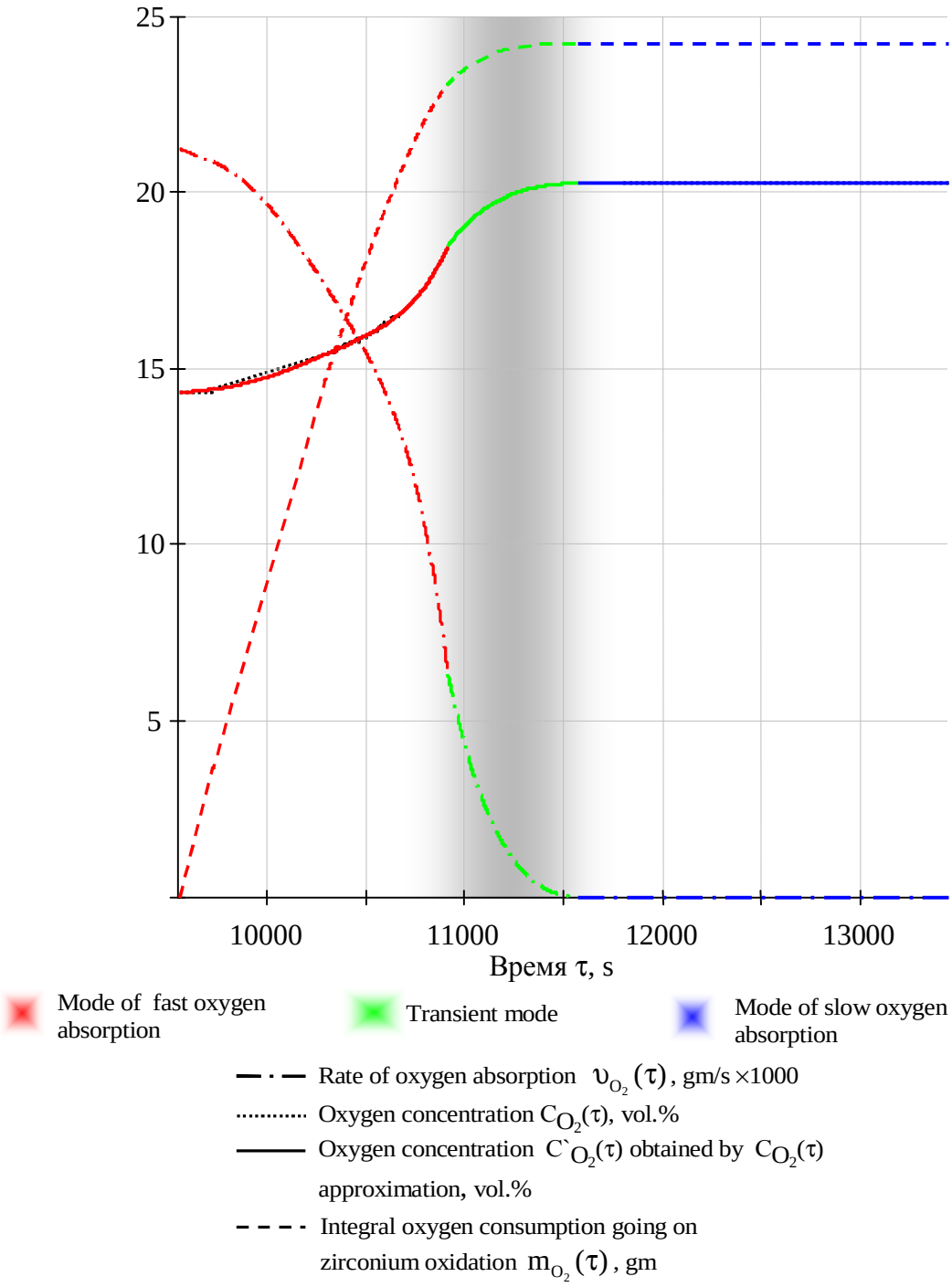

Fig. 19. Calculation of the oxygen absorption rate, assuming two mechanisms

Table 9

Summary table of calculated results

Period No.	Period duration Dt, h	Air consumption, l/sec	Mass of absorbed oxygen m_{O_2}, g	Mass of Zr in oxidic form (ZrO_2) in the melt, g	Mass of non-oxidized Zr in the melt, g	Corium index – C
1	0.45	0.04	9.28	115.71	169.37	40.59
2	0.49	0.07	15.24	159.16	125.92	55.83
3	0.84	0.17	20.35	217.17	67.91	76.18
4	1.08	0.25	22.61	281.63*	3.45*	98.79*
5	0.64	0.41	0	285.08	0	0

*). According to the calculation, the absorption of atmospheric oxygen by the melt stopped at 11,579 sec (0.56 h into the 4th steady-state regime). At the same time, both the calculations and chemical analysis of the melt samples show (Tab. 3) that a small amount of zirconium remained suboxidized. These discrepancies may be explained by the error of oxygen determination during all the steady-state regimes, accuracy of determining the melt composition prior to supplying air into the furnace, changing rate of the melt evaporation with the growth of its temperature, approximation error, etc.

Conclusion

1. The work performed on modernizing the Rasplav-3 test facility made it possible to superheat the melt above T_{liq}. within a broad range of oxygen potentials (and hence, electrical conductivities of the melt), which correspond to variation of the oxidation index from C-30 to C-100+.
2. A technique of studying the melt oxidation kinetics using the results of the oxygen partial pressure measurements at the furnace outlet has been tested.
3. The first experimental data on the suboxidized molten corium oxidation kinetics, essential for oxidation modelling, have been obtained.
4. The melt oxidation was found to be accompanied by such qualitative effects as:
   - swirling and splashing,
   - surface heating.
5. A higher (compared to the Project Phase 1) heat flux into the molten pool bottom has been recorded, which proves the necessity of an additional test to study the molten pool hydrodynamics employing the Rasplav-3 test facility which has a considerably lower (than Rasplav-2) generator current frequency.

References

1. D. Lopukh, S. Bechta, A. Pechenkov, S. Vitol, K. Froment, S. Hellmann, M. Ficsher, B. Duret, J.M. Seiler. New experimental results on the interaction of molten corium with core catcher materials. Proceedings of ICONE-8 8th International Conference on Nuclear Engineering, April 2-6, 2000, Baltimore, MD USA, ICONE-8179.
2. Losev N.F. Quantitative X-ray fluorescence spectroscopy. M.:Nauka, 1969, 366 p.
3. RASPLAV Final Report. Attachment A. Post-test Examinations Methodology and Results Data published – July, 2000.
4. Khabensky V.B. et al. Techniques of physico-chemical analyses // Progress report. NITI, MC-02/99, July 1999.